Numerical Simulations of Unsteady Transonic Flow in Diffusers

Meng-Sing Liou*
National Cheng Kung University, Tainan, Taiwan, China
and
Thomas J. Coakley†
NASA Ames Research Center, Moffett Field, California

Forced and self-excited oscillations of transonic flows in two-dimensional diffusers were numerically simulated using the Reynolds-averaged compressible Navier-Stokes equations. Depending on the shock strengths and the area ratios, the character of the flows ranged from fully attached to largely separated. In the case of forced oscillations, a harmonic pressure wave was prescribed at the exit plane. Solution data over several cycles of quasiperiodic motion were analyzed by spectral methods. Comparisons of computed and experimental results generally gave good to very good agreement for the forced oscillation cases and fair to good agreement for the self-excited oscillation cases.

Introduction

UNSTEADINESS in the flowfield, either naturally present or externally forced, frequently causes undesirable distortions and performance losses in aircraft and missile inlets. The engineering problems associated with inlet distortions have been extensively documented.[1,2] However, the physical mechanisms involved are not well understood. Extensive experimental investigations of unsteady transonic flows have been made.[3-8] Meier[3] used high-speed interferometry to investigate the flow in a Laval nozzle and found a nearly periodic, pulsating flow that was governed by complicated interactions between the shock wave and the separated boundary layer. Sajben and his associates investigated a variety of nominally two-dimensional transonic diffuser flows.[4-8] Both fully attached and separated flows were investigated and both shock-induced and pressure-gradient-induced separations were observed. Natural or self-excited oscillations were found in all test flows. Forced oscillations, produced by mechanically induced perturbations, were studied in great detail using a laser velocimeter, pressure probes, and a line-scan imaging camera for tracking the shock wave locations.

Theoretical analysis has focused primarily on unsteady inviscid flows in varying area channels.[9-11] In Ref. 11, the large-amplitude shock motion, subject to perturbations imposed at the channel exit, was analyzed. Since the boundary-layer thickness increases significantly through a shock wave and in the subsequent divergent section of a diffuser, viscous interaction effects can be substantial. A procedure of coupling the inviscid and viscous solutions was presented in Ref. 12. A simple theoretical modeling of pressure oscillations in ramjets was formulated in Ref. 13 using acoustic analysis. However, there have been very few theoretical or numerical studies of unsteady separated flows in transonic diffusers, although some relevant work has been done for airfoils.[14,15]

The purpose of the present investigation was to numerically simulate several of the diffuser flows documented by Sajben and his associates.[4-8] The flows in two diffuser models, labeled G and B in Fig. 1, were simulated. The flows in model G contained mechanically produced or forced oscillations. Two of these flows were simulated: the first contained a relatively strong shock wave and was separated and the second contained a weak shock wave and was unseparated. The model B flows all contained naturally occurring or self-excited oscillations and were separated. Three of these flows were simulated. The first two were separated at the shock wave, while the third was separated by the adverse pressure gradient in the divergent section of the diffuser.

Because the unsteady and separated features of these flows were of such importance, only numerical methods capable of solving the time-dependent Reynolds-averaged compressible Navier-Stokes equations were considered. The computer code developed by Coakley and Bergmann[16] utilizing MacCormack's hybrid method[17] and various turbulence models was used initially to solve several shock-separated flows. Subsequent applications[18] to several of the present diffuser flows resulted in successful predictions of steady or mean flow details such as pressure distributions, the size and extent of separation, mean velocity profiles, and shock wave locations and patterns. The present paper represents a more ambitious application to the unsteady aspects of those flows.

In the following presentation, brief descriptions will be given of the equations of motion, the turbulence model, and the numerical method used in the simulations. These will be followed by a discussion of results, which includes detailed comparisons with experimental data.

Equations of Motion

The equations used to describe viscous turbulent flows at high speeds are the Reynolds-averaged compressible Navier-Stokes equations. These equations are obtained from the basic Navier-Stokes equations using an averaging process called density- or mass-weighted time averaging[19] (or Favre averaging). This type of averaging results in a set of equations having essentially the same form as the basic equations but with molecular stresses and fluxes replaced by total stresses and fluxes that include both molecular and turbulent contributions. The averaged equations are rigorously applicable only to steady flows, but they may also be applied to unsteady flows if the frequencies of the bulk unsteady motions are much smaller than the dominant frequencies of the turbulent motions. This is an inherent assumption upon which the present investigation rests.

Presented as Paper 82-1000 at the AIAA/ASME Third Joint Thermophysics, Fluids, Plasma and Heat Transfer Conference, St. Louis, Mo., June 7-11, 1983; submitted June 17, 1982; revision received Oct. 19, 1983.

*Professor, Department of Aeronautical Engineering. Member AIAA.

†Research Scientist. Member AIAA.

The equations are expressed here in conservation form and in general curvilinear coordinates using the finite volume formulation.[16] In vector/dyadic form, the equations for the conservation of mass, momentum, and energy are written, respectively, as

$$\partial_t \rho v + \partial_i \rho \boldsymbol{u} \cdot \boldsymbol{S}_i = 0 \tag{1a}$$

$$\partial_t \rho \boldsymbol{u} v + \partial_i (\rho \boldsymbol{u}\boldsymbol{u} + \vec{\sigma}) \cdot \boldsymbol{S}_i = 0 \tag{1b}$$

$$\partial_t \rho E v + \partial_i (\rho E \boldsymbol{u} + \boldsymbol{u} \cdot \vec{\sigma} + \boldsymbol{q}_e) \cdot \boldsymbol{S}_i = 0 \tag{1c}$$

where $\partial_t = \partial/\partial t$ and $\partial_i = \partial/\partial \xi_i$ are partial derivatives with respect to time and space, respectively, and the summation convention is used for repeated subscripts. The variables ξ_i, $i = 1, 2, 3$ are curvilinear coordinates that are related to the Cartesian coordinate variables x_i by the transformation

$$\boldsymbol{r} = x_i \boldsymbol{e}_i = X_i(\xi_i)\boldsymbol{e}_i \tag{2}$$

where $\boldsymbol{e}_i$ are Cartesian unit base vectors and $\boldsymbol{r}$ the coordinate vector.

The geometric variables in Eq. (1) are the differential volume element v and the differential surface element vector $\boldsymbol{S}_i$. These variables are related to the coordinate vector by

$$\boldsymbol{S}_i = (\partial_j \boldsymbol{r}) \times (\partial_k \boldsymbol{r}) \tag{3a}$$

$$v = (\partial_i \boldsymbol{r}) \cdot (\partial_j \boldsymbol{r}) \times (\partial_k \boldsymbol{r}) \tag{3b}$$

where the symbols $(\cdot)$ and $\times$ represent vector dot and cross products, respectively, and a cyclic permutation of the indices i, j, and k is assumed.

The (averaged) physical variables are the density ρ, the Cartesian velocity vector $\boldsymbol{u} = u_i \boldsymbol{e}_i$, and the specific total energy $E = e + \frac{1}{2}\boldsymbol{u}\cdot\boldsymbol{u}$, where e is the specific internal energy. An ideal gas is assumed so that the equation of state can be written, $p = (\gamma - 1)\rho e$, where p is the thermodynamic pressure and γ the ratio of specific heats. The total stress tensor, including both molecular and turbulent contributions, is represented by

$$\vec{\sigma} = (p + \tfrac{2}{3}\rho k)\vec{I} - \frac{\mu_v}{v}\left[\boldsymbol{S}_j(\partial_j \boldsymbol{u}) + (\partial_j \boldsymbol{u})\boldsymbol{S}_j - \tfrac{2}{3}\vec{I}\boldsymbol{S}_j \cdot \partial_j \boldsymbol{u}\right] \tag{4}$$

where k is the mass-averaged turbulent kinetic energy, i.e., $k = \overline{\rho u_i'' u_i''}/\bar{\rho}$, and $\vec{I} = \boldsymbol{e}_i \boldsymbol{e}_j \delta_{ij}$ is the unit tensor or dyadic. The total thermal flux vector is represented in a similar fashion,

$$\boldsymbol{q}_e = -\frac{\mu_e}{v}\boldsymbol{S}_j \partial_j u \tag{5}$$

Equations (4) and (5) are based on the Boussinesq approximation, or the eddy viscosity hypothesis, in which the combined viscosity coefficient μ_v is given by the sum of the molecular viscosity μ and a turbulent viscosity μ_T. The combined thermal conductivity is defined similarly so that μ_v and μ_e are expressed by

$$\mu_v = \mu + \mu_T, \qquad \mu_e = \gamma(\mu/Pr + \mu_T/Pr_e) \tag{6}$$

where Pr and Pr_e are the molecular and turbulent Prandtl numbers, respectively. The molecular Prandtl number for air is $Pr = C_p\mu/\kappa = 0.72$ and Pr_e is given in the following section.

To improve computational efficiency without seriously compromising physical accuracy, an approximate form called the thin-layer Navier-Stokes equations is used.[20] These equations are obtained from Eqs. (1), (4), and (5) by discarding derivatives involving viscous terms in the streamwise direction (i.e., $\xi = \xi_1$). For the purpose of this investigation, the equations are further simplified by assuming two-dimensional plane flow.

Turbulence Models

Turbulence closure of the basic equations is achieved by specifying the eddy viscosity μ_T in terms of known field quantities and/or additional field variables. For the present investigation, the two-equation turbulence model of Wilcox and Rubesin[21] is used. In this model, two additional field equations are solved, one for the turbulent kinetic energy k and the other for the specific dissipation rate of kinetic energy. The eddy viscosity is expressed as a function of these variables as described below. Written in conservation form, the equations for k and ω^2 are

$$\partial_t \rho k v + \partial_i (\rho k \boldsymbol{u} + \boldsymbol{q}_k) \cdot \boldsymbol{S}_i = H_k \tag{7a}$$

$$\partial_t \rho \omega^2 v + \partial_i (\rho \omega^2 \boldsymbol{u} + \boldsymbol{q}_{\omega^2}) \cdot \boldsymbol{S}_i = H_{\omega^2} \tag{7b}$$

where the flux vectors $\boldsymbol{q}_k$ and $\boldsymbol{q}_{\omega^2}$ are expressed in the same form as Eq. (5), and the corresponding combined viscosity coefficients are given by

$$\mu_k = \mu + \mu_T/Pr_k, \qquad \mu_{\omega^2} = \mu + \mu_T/Pr_{\omega^2} \tag{8}$$

The functions H_k and H_{ω^2} are turbulent source functions, i.e.,

$$H_k = \mu_T S - 0.09\rho v \omega k \tag{9a}$$

$$H_{\omega^2} = [\bar{\gamma}\mu_T S - (0.15 + \ell_\sigma^2)\rho v \omega k]\,\omega^2/k \tag{9b}$$

where

$$\ell_\sigma = v^{-1} S_\eta \partial_\eta (\sqrt{k}/\omega) \tag{10a}$$

$$S = v^{-1} S_\eta^2 [4/3(\partial_\eta v')^2 + (\partial_\eta u')^2] \tag{10b}$$

In these equations, $\eta = \xi_2$ is the coordinate variable that is (approximately) normal to the flow direction or diffuser walls, $\partial_\eta = \partial/\partial_\eta = \partial/\partial\xi_2$, and $S_\eta = |\boldsymbol{S}_2|$. The velocity components v' and u' are parallel and perpendicular, respectively, to $\boldsymbol{S}_\eta$, e.g., $v' = \boldsymbol{u}\cdot\boldsymbol{S}_\eta/S_\eta$. Equations (9b) and (10b) are simplified forms resulting from the thin-layer approximation.

The eddy viscosity is defined by

$$\mu_T = \rho\gamma^* k/\omega \tag{11}$$

and the closure parameters in Eqs. (6), (8), (9), and (11) are

$$\gamma^* = 1 - 0.9917\exp(-\rho k/\mu\omega) \tag{12a}$$

$$\bar{\gamma} = \gamma_\infty [1 - 0.9917\exp(-0.5\rho k/\mu\omega)]/\gamma^* \tag{12b}$$

$$\gamma_\infty = 10/9, \quad Pr_e = 9/10, \quad Pr_k = Pr_{\omega^2} = 2 \tag{12c}$$

The turbulence model described above is relatively sensitive to the choice of the constant γ_∞ in Eq. (12). In most of the calculations reported here and in Ref. 18, the originally proposed value of $\gamma_\infty = 10/9$ was used.[21] This differs from the recommendation of Ref. 22 where the value $\gamma_\infty = 9/10$ gave slightly better predictions of skin friction for attached flows (using Navier-Stokes codes). It was found in Ref. 18, however, that the original value, $\gamma_\infty = 10/9$, consistently gave better predictions of separated flows. An exception to this usage was for the most extensively separated flow of the model B diffuser (i.e., $R_p = 0.74$). In this case, it was necessary to use a reduced value, i.e., $\gamma_\infty = 9/10$, in the neighborhood and downstream of the reattachment point. This procedure was required to prevent the separation zone from extending beyond the exit plane of the diffuser, an occurrence that was inconsistent not only with the experimentally observed extent of separation but also with the numerical boundary conditions used. The procedure has been adopted in the present investigation (for $R_p = 0.74$).

Some sensitivity with respect to the choice of the Prandtl numbers, Pr_k and Pr_{ω^2}, in Eq. (12) was also reported in Ref. 18. In that reference, the values $Pr_k = Pr_{\omega^2} = 1$ were found to give better predictions of the top wall pressure distributions for the model G diffuser than the original values given by Eq. (12). In this investigation, however, we have elected to use the constants of Eq. (12) in order to maintain a higher degree of consistency with the model as originally proposed.

Numerical Method

The numerical method used to solve the equations is basically MacCormack's hybrid method[17] with modifications to improve its efficiency and flexibility.[16] If the column vector of state variables, $U=\rho v(1,u,E,k,\omega^2)$, is known at time t, then the solution at time $t+\Delta t$ is obtained from the operational formula

$$U(t+\Delta t) = L(\Delta t)\, U(t) \tag{13}$$

The numerical operator $L(\Delta t)$ is represented as a product of simpler operators utilizing the technique of time splitting

$$L(\Delta t) = L_\xi^i(\Delta t)\, L_\eta^i(\Delta t)\, L_\eta^v(\Delta t) \tag{14}$$

In this expression, the subscripts $\xi(=\xi_1)$ and $\eta(=\xi_2)$ refer to coordinate directions in which the associated operator is applied, and the superscripts i and v refer to subsets of the inviscid and viscous equations associated with each coordinate direction. In the streamwise direction, the viscous operator L_ξ^v is not used, which is in accordance with the thin-layer approximation. Specific details on the construction of these operators are given in Ref. 16.

The specification of numerical boundary conditions is based on a method-of-characteristics construction generalized to include viscous effects. At the diffuser top and bottom walls, the no-slip condition, $u=0$, is imposed. The wall pressures are computed utilizing a characteristics-type construction and the turbulent kinetic energy is set to zero, i.e., $k=0$. The specific dissipation rate of turbulent kinetic energy, i.e., ω, is specified by an analytic formula at the first few points adjacent to each wall (i.e., $\omega = 133\mu/\rho y^2$).

At the diffuser inlet, in the core flow region, the total temperature and entropy are prescribed (constant), the vertical velocity is set to zero ($v=0$), and the static pressure and horizontal velocity u are obtained from a characteristics construction. In the thin boundary-layer regions adjacent to the walls, the total temperature is prescribed along with nondimensional turbulent velocity profile functions for u/u_e. The physical u velocities are obtained by scaling the profile functions with the core flow velocity. The turbulence variables k and ω are prescribed by suitable profile functions. Corresponding to experimental values, the inlet boundary-layer thicknesses for model G were specified as 9 and 4.5% of the diffuser height at the top and bottom walls, respectively. For model B, the respective thicknesses were 6 and 2%.

At the diffuser exit boundary, the static pressure was prescribed and the u velocity was determined by a characteristics construction. Consistent with characteristics theory, the entropy, v velocity, and turbulence variables were determined from values adjacent to the boundary by a zero gradient condition, i.e., $\partial f/\partial\xi = 0$. More details on the above boundary conditions may be found in Ref. 16.

The computational meshes used for the two models were body-fitted, analytically generated H grids. For the model G diffuser a mesh of 80×50 cells was used with 80 cells in the streamwise direction. For the model B diffuser, the mesh contained 90×60 cells. In order to capture details of the shock wave patterns, a uniformly spaced fine mesh with $\Delta X/H^* \approx 1/15$ was used in the shock zone in the streamwise directions ξ. In the cross-stream direction η, the meshes were exponentially expanded away from each wall and were joined to a uniformly spaced mesh in the core flow region. The

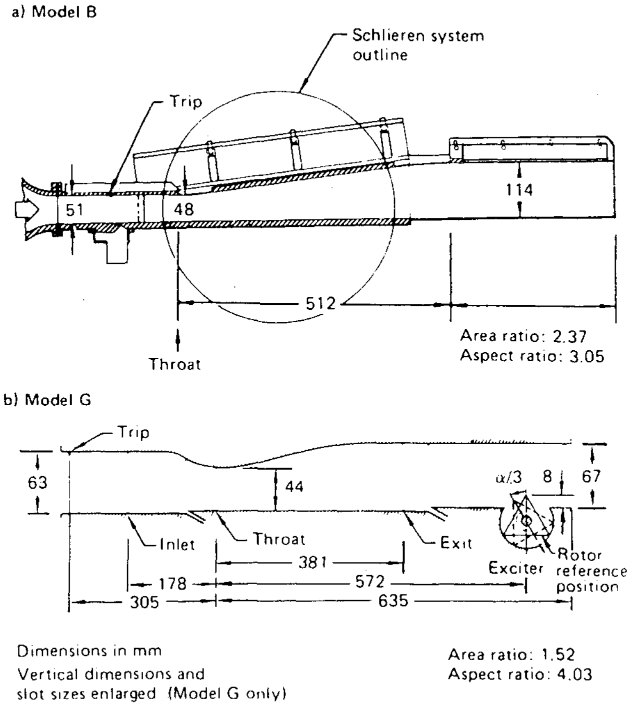

Fig. 1 Diffuser configurations.

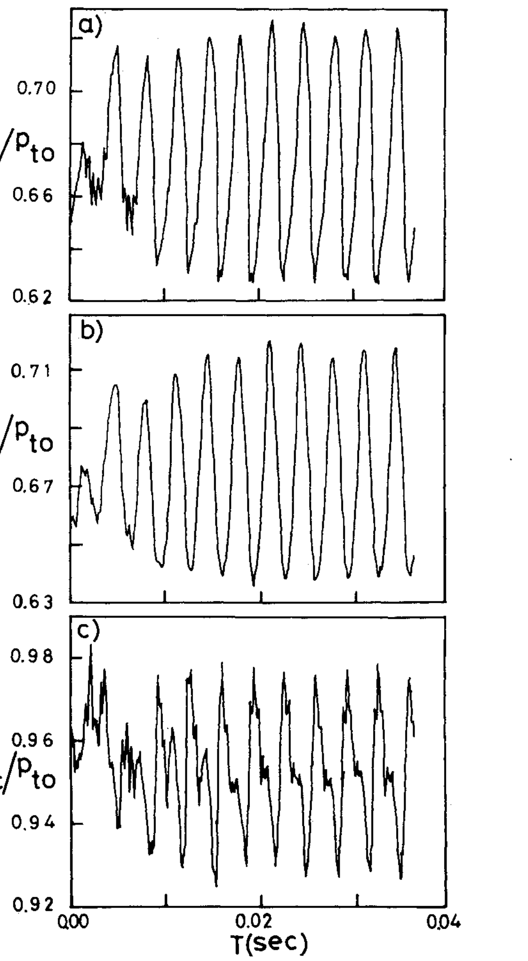

Fig. 2 Time histories for a) top wall static pressure, b) core static pressure, and c) core total pressure at $X/H^* = 5.836$ (model G, $R_p = 0.72$).

values of y^+ at the first row of points adjacent to each wall were generally well within the viscous sublayers, i.e., $y^+ < 5$.

The computing times for the two sets of calculations were as follows. For the G diffuser, approximately 20 min on the Ames CDC 7600 computer were required to compute one cycle of oscillation that took 860 time steps. Since a total of 10-11 cycles were computed, the total computing time was approximately 3.5 h per case. For the B diffuser about 6 h were required for each case, which included roughly 7-9 cycles of self-excited (transient plus quasiperiodic) oscillations.

Results

Results for the model G diffuser forced oscillations will be discussed first followed by a discussion of the model B natural oscillations. In both cases, a sufficient number of cycles were computed so that the initial (two to four) transient cycles could be discarded, leaving several quasiperiodic cycles available for spectral analysis. The basic parameter characterizing these flows is the diffuser pressure ratio R_p, which is the ratio of the mean static exit pressure to the plenum (total) pressure, i.e., $R_p = p_e / P_{To}$. In the figures to be discussed, H^* represents the diffuser-throat height and X the horizontal distance measured from the throat.

Forced Oscillations, Model G

In the model G experiments, the forced oscillations were generated by a triangular rotor placed in the exit section (see Fig. 1). In the numerical computations, this effect was simulated by taking the exit pressure to be a harmonic function of time, i.e., $P_{et} = P_e + P_e' \sin 2\pi\omega t$, where P_e' is the amplitude of the oscillation and ω the frequency. The frequency was set at $\omega = 300$ Hz, which was representative of the experimental test flows. The amplitudes were set at $P_e'/P_e = 0.011$ and 0.010. These were the approximate amplitudes of the experimental pressure oscillations at the forcing frequency (i.e., the first harmonic) measured at the exit station, $X/H^* = 8.65$ (see Fig. 1).

Two flows were computed. The first, with $R_p = 0.72$, contained a relatively strong shock wave and shock-induced separation and the second, with $R_p = 0.80$, contained a weak shock wave and no separation.

Strong Shock, $R_p = 0.72$

At this pressure ratio, a fairly extensive region of separated flow along the top wall of the diffuser exists over much of the oscillation cycle. Computed time histories of the top wall and core flow static pressures and the core flow total pressures at a location of $X/H^* = 5.836$ are shown in Fig. 2. This is the approximate location of reattachment. The initial transients took about three cycles to die out and about seven quasiperiodic cycles were available for analysis. An interesting feature of these time histories is that the total pressure oscillations have a considerably higher frequency content than the static pressure oscillations.

Measured and computed mean pressure distributions are compared in Fig. 3. Core flow static and total pressures are compared in Fig. 3a and the top wall static pressures in Fig. 3b. The computed core flow pressures show very good agreement with measurements. The computed top wall pressures are in good agreement with measurements near the shock and exit regions of the flow, but show a slightly higher recovery in the region downstream of the shock wave. As mentioned in the section on turbulence modeling, better agreement can be achieved in this case by using modified constants (i.e., $Pr_k = Pr_{\omega^2} = 1$), but this modification was not used in the present investigation.

Computed power spectra for the core flow static pressures at two streamwise locations are shown in Fig. 4. The spectra at the location $X/H^* = 5.836$ (i.e., reattachment) shows a single dominant component at the forcing frequency (300 Hz), whereas the spectra at $X/H^* = 4.321$, which is within the separation zone, shows significant additional frequency components at 100 and 600 Hz.

Amplitude and phase distributions of the core flow static and total pressure oscillations at the forcing frequency (or first harmonic) are shown in Fig. 5. The amplitudes are normalized by the amplitude of the exit pressure oscillation (i.e., P_e'). These comparisons generally indicate very good agreement between computation and experiment. An important feature is the nodal point at $X/H^* = 4.0$ where the static pressure amplitude becomes small and the phase changes rapidly through an angle of (approximately) 180 deg. Since the power spectra taken near this point (see Fig. 4, $X/H^* = 4.321$) show the presence of significant additional frequency components, nonlinear effects may be important here. Another feature of interest is the relatively large amplification of static pressure near the shock wave ($X/H^* \approx 3$) and the reattachment point ($X/H^* \approx 6$). Finally, the entirely different behavior of the total pressure distributions should be noted. This includes the absence of nodal points, no rapid changes in phase angle (except at the shock for the computed

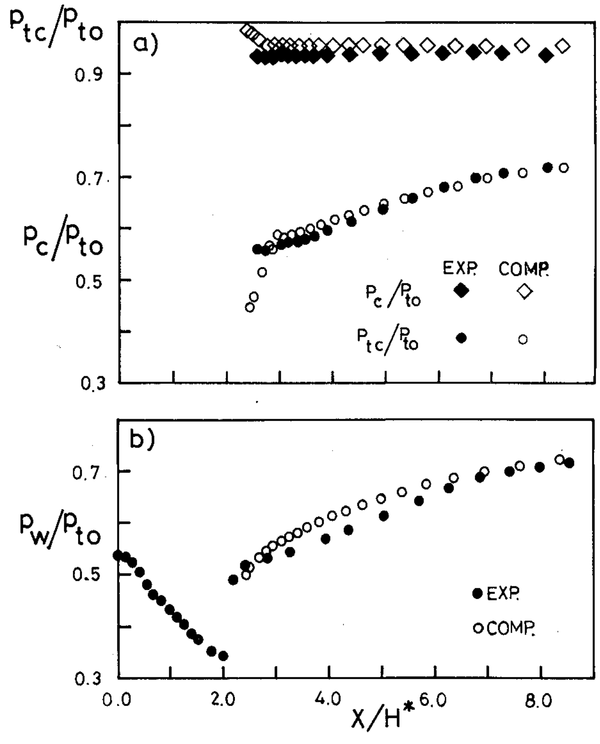

Fig. 3 Mean streamwise distribution for a) static and total pressure in the core region and b) top wall static pressure (model G, $R_p = 0.72$).

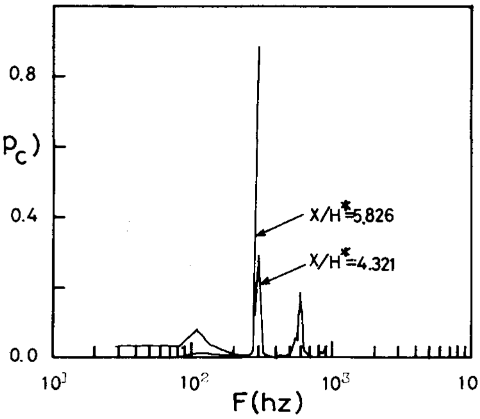

Fig. 4 Power spectral density for core static pressure fluctuations at $X/H^* = 4.321$ and 5.836 (model G, $R_p = 0.72$).

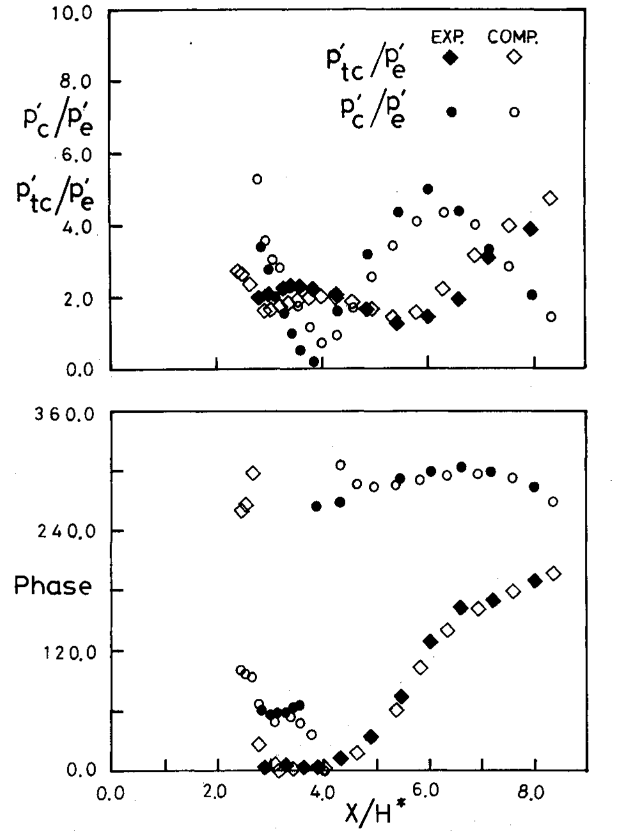

Fig. 5 Streamwise distribution of amplitude and phase angle for the first harmonic (300 Hz) fluctuations of core, static, and total pressures (model G, $R_p = 0.72$).

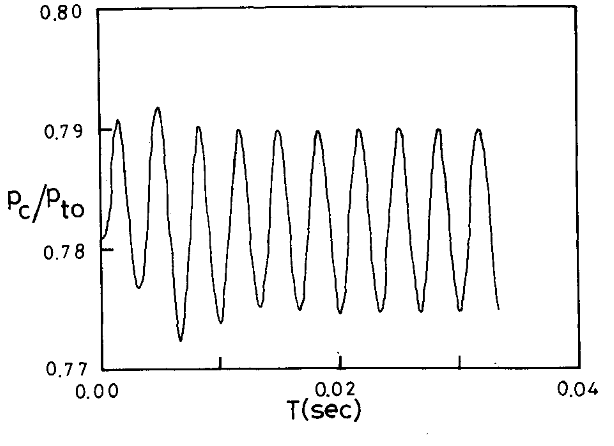

Fig. 6 Time history of core static pressure at $X/H^* = 5.836$ (model G, $R_p = 0.8$).

phase angles only), and a relatively large amplification at the exit plane where the static pressure amplitudes are small.

Weak Shock, $R_p = 0.80$

At this pressure ratio the flow is unseparated throughout the diffuser. A time history of the computed core flow static pressure at $X/H^* = 5.836$ is shown in Fig. 6. In this case the pressure oscillation is smoother and more nearly sinusoidal than in the strong shock case (Fig. 2b). The time histories for the total pressure and static wall pressure (not shown) indicated a similar behavior.

The calculations for this case were done at the pressure ratio, $R_p = 0.80$, whereas the nearest experimental pressure ratio investigated was $R_p = 0.82$. Thus, the computed mean pressure distributions (corresponding to Fig. 3 but not shown here), although in excellent qualitative agreement, showed a small downward displacement with respect to the measurements.

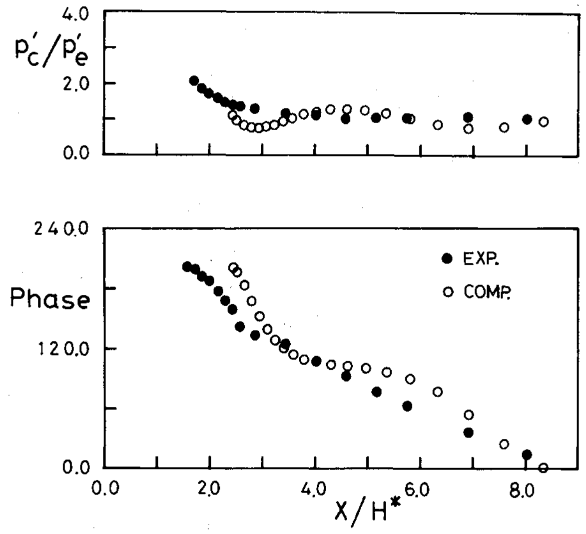

Fig. 7 Streamwise distribution of amplitude and phase angle for the first harmonic (300 Hz) fluctuations of core static pressure (model G, $R_p = 0.8$).

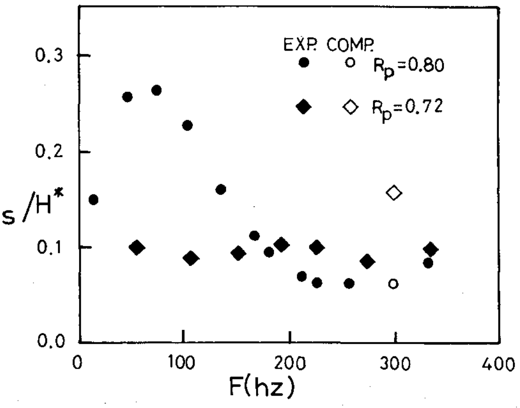

Fig. 8 Shock rms displacement amplitude vs frequency (model G).

Streamwise amplitude and phase distributions for the first harmonic of the core flow static pressure oscillations are shown in Fig. 7. Agreement between the computed and experimental results is generally good. In contrast to the strong shock case (i.e., Fig. 5), there are no nodal points or regions of significant amplification in the amplitude distributions, nor are there any rapid changes in the phase distributions.

Experimental and computational rms shock displacement amplitudes for the strong and weak shock cases are compared in Fig. 8. Agreement is very good for the weak shock case but, in the strong shock case, the computed amplitudes are about 60% higher than the experimental amplitudes. We were unable to find an explanation for this disparity in light of the good agreement found elsewhere in the comparisons.

Natural Oscillations, Model B

In the model B experiments, natural or self-excited oscillations were observed. These oscillations were relatively small and not of the large pulsating type observed in some experiments.[13,14] Three flows were selected for numerical simulation. They are discussed below as the strong, moderate, and weak shock cases. The first two flows were separated

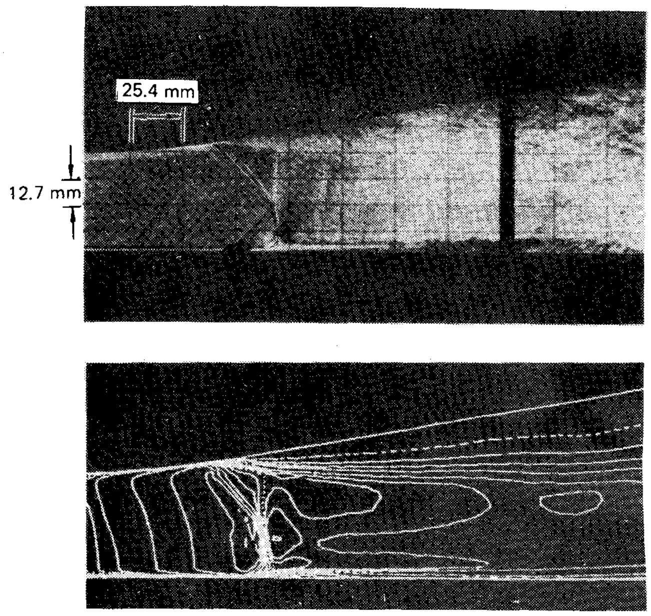

Fig. 9 Schlieren photograph and computed Mach number contour, (model B, $R_p = 0.74$).

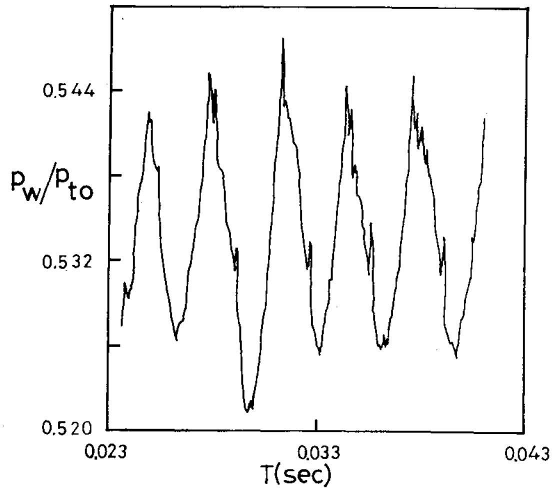

Fig. 10 Time history of top wall static pressure at $X/H^* = 2.0$ (model B, $R_p = 0.74$).

(along the top wall) by the shock wave, while the third was separated by the adverse pressure gradient in the divergent section.

In the numerical simulations, the static pressure was held constant at the exit boundary. The computation times for these cases were greater than those for the G diffuser; thus, only 3-5 quasiperiodic cycles were available for analysis. Although small, this number was deemed sufficient for the purposes of the investigation.

Strong Shock, $R_p = 0.74$

In this case, the pressure ratio was sufficient to cause a bifurcated- or lambda (λ)-type shock wave and an extensive zone of separation. Computed Mach contours are shown with a Schlieren photograph of this flow in Fig. 9. The bifurcated character of the shock wave is well predicted by the computations.

A computed time history of the top wall pressure oscillation, at a location of $X/H^* = 2$, is shown in Fig. 10. This location is slightly downstream of the mean shock wave position. Spectral analysis of the shock wave and pressure oscillations showed a dominant frequency of 290 Hz, which was about 75% greater than the measured frequency of 165 Hz.

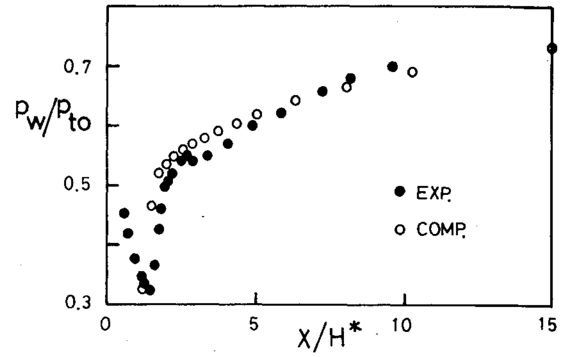

Fig. 11 Mean streamwise distribution of top wall static pressure (model B, $R_p = 0.74$).

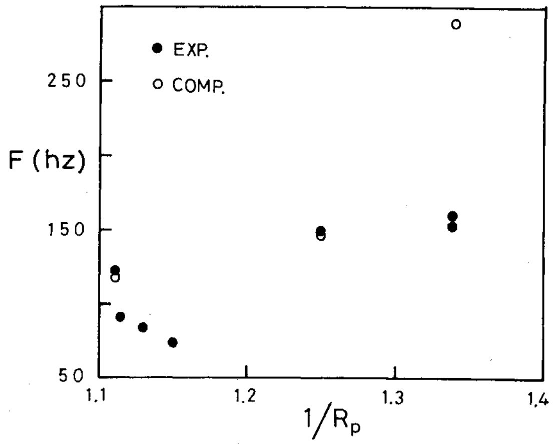

Fig. 12 Pressure ratio dependence of dominant frequency for shock motion in model B diffuser.

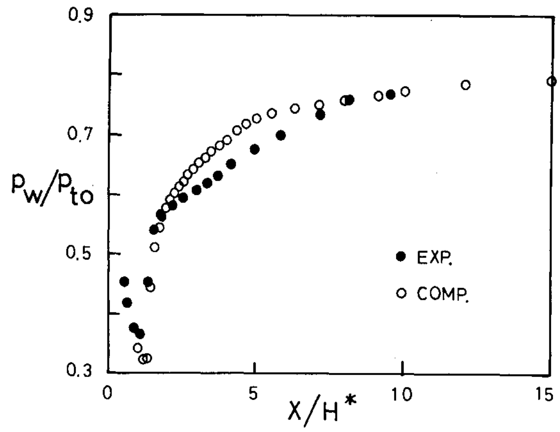

Fig. 13 Mean streamwise distribution of top wall static pressure (model B, $R_p = 0.8$).

Measured and computed mean pressure distributions along the top wall are compared in Fig. 11. The agreement between computation and experiment in this case is generally good, although the predicted distributions do show a slightly greater recovery downstream of the shock wave.

Moderate Shock, $R_p = 0.8$

At this pressure ratio, the shock wave was curved but not bifurcated, and the flow contained a fairly extensive zone of separation.[18] Spectral analysis of the shock wave motion showed a dominant frequency of 148 Hz, which was very close to the measured value of 150 Hz (see Fig. 12). Mean

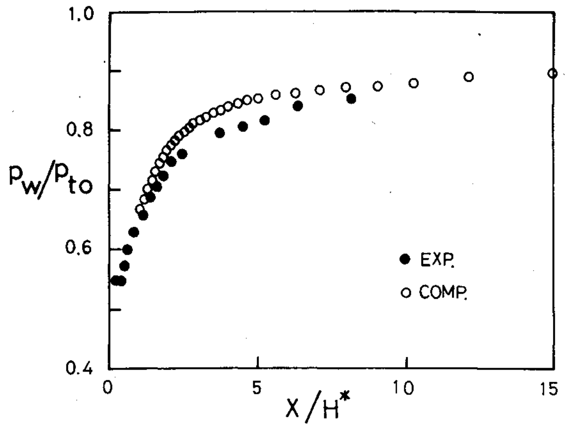

Fig. 14 Mean streamwise distribution of top wall static pressure (model B, $R_p = 0.9$).

pressure distributions along the top wall are shown in Fig. 13. Although the experimental location of the shock wave was well predicted, the behavior mentioned above with regard to overprediction of pressures downstream of the shock was more pronounced.

Weak Shock, $R_p = 0.9$

The experimental flow in this case contained a weak shock wave located close to the diffuser throat and a pressure-gradient-induced separation that occurred at some distance downstream ($X/H^* \approx 2.5$). The dominant frequency of the computed shock wave oscillation was 116 Hz, which was close to the experimental value of 122 Hz (see Fig. 12). The computed and experimental pressure distributions shown in Fig. 14 indicate about the same level of agreement as attained in the moderate shock case.

Conclusions

We have numerically simulated a series of unsteady transonic diffuser flows with the aim of predicting experimental measurements. Two kinds of unsteady flows were investigated. These were the forced oscillations of the model G diffuser and the natural or self-excited oscillations of the model B diffuser. The numerical simulations were generally successful in predicting the unsteady forced oscillations. Important differences in behavior were found between the separated and unseparated cases. In the unseparated or weak shock case, the oscillations were relatively mild and uncomplicated. This tends to support the opinion that unseparated flows can be predicted by methods simpler[12] and more efficient than the one used here. In the separated or strong shock case, the flow oscillations were more severe and complicated. This tends to indicate that simpler methods will be less successful in these cases.

The numerical predictions of the natural oscillations of the model B diffuser flows were in fair to good agreement with measurements. In the moderate and weak shock cases, the natural frequencies were well predicted, but the mean pressure distributions were not as well predicted. In the strong shock case, the pressure distributions were fairly well predicted, but the natural frequency was (75%) too high. These flows posed a more difficult numerical challenge than did the model G flows because they contained more extensive regions of separation and three-dimensionality. The fact that they contained more extensive regions of separation brings turbulence modeling more into question, since the present models are not yet well developed in these cases. Although improvements in predictions can be achieved through modifications of the modeling constants,[18] these modifications have not yet been systematized for a wide range of separated flows. The presence of three-dimensionality in the experimental flows brings into question the applicability of two-dimensional simulations. Although three-dimensional unsteady turbulent flow simulations can be made, they are presently impractical from the standpoint of computing time. Thus, in light of these questions, we feel the numerical simulations were reasonably successful in predicting the basic features of the unsteady natural oscillations.

Acknowledgment

This research was supported initially by the McDonnell Douglas Independent Research and Development Program and later by the NASA Ames Research Center. The authors would like to acknowledge useful suggestions from one of the reviewers.

References

[1] "Propulsion System Flow Stability Program (Dynamics)," AFAPL-TR-68-142, 1968.

[2] "Supersonic Inlet Design and Airframe-Inlet Integration Program (Project Tailor Mate)," AFFDL-TR-71-124, 1973.

[3] Meier, G. E. A., "Shock Induced Flow Oscillations," *Flow Separation,* AGARD CP 168, 1974.

[4] Sajben, M., Kroutil, J. C., and Chen, C. P., "Unsteady Transonic Flow in a Two-Dimensional Diffuser," *Unsteady Aerodynamics,* AGARD CP 227, 1977, pp. 13-1/13-14.

[5] Chen, C. P., Sajben, M., and Kroutil, J. C., "Shock Wave Oscillations in a Transonic Diffuser Flow," *AIAA Journal,* Vol. 17, Oct. 1977, pp. 1076-1083.

[6] Salmon, J. T., Bogar, T. J., and Sajben, M., "Laser Velocimeter Measurements in Unsteady, Separated, Transonic Diffuser Flows," AIAA Paper 81-1197, 1981.

[7] Bogar, T. J., Sajben, M., and Kroutil, J. C., "Characteristic Frequencies and Length Scales in Transonic Diffuser Flow Oscillations," AIAA Paper 81-1291, 1981.

[8] Sajben, M., Bogar, T. J., and Kroutil, J. C., "Forced Oscillation Experiments in Supercritical Diffuser Flows with Application to Ramjet Instabilities," AIAA Paper 81-1487, 1981.

[9] Jacob, D., "On some Aspects of Shock Wave Oscillations in Supersonic Diffusers," Ph.D. Thesis, University of Tennessee Space Institute, Tullahoma, Tenn., 1968 (summary in AFFDL-TR-69-103).

[10] Adamson, T. C. Jr., "Unsteady Transonic Flows in Two-Dimensional Channels," *Journal of Fluid Mechanics,* Vol. 52, 1972, pp. 437-449.

[11] Adamson, T. C., Jr., Messiter, A. F., and Liou, M-S., "Large Amplitude Shock-Wave Motion in Two-Dimensional, Transonic Channel Flows," *AIAA Journal,* Vol. 16, Dec. 1978, pp. 1240-1247.

[12] Liou, M-S. and Sajben, M., "Analysis of Unsteady Viscous Transonic Flow with a Shock Wave in a Two-Dimensional Channel," AIAA Paper 80-0195, 1980.

[13] Culick, F. E. C., and Rogers, T., "Modeling Pressure Oscillations in Ramjets," AIAA Paper 80-1192, 1980.

[14] Levy, L. L. Jr., "Experimental and Computational Steady and Unsteady Transonic Flows about a Thick Airfoil," *AIAA Journal,* Vol. 16, June 1978, pp. 564-572.

[15] Tijdeman, H. and Seebass, R., "Transonic Flow Past Oscillating Airfoils," *Annual Review of Fluid Mechanics,* Vol. 12, 1980, pp. 181-222.

[16] Coakley, T. J. and Bergmann, M. Y., "Effects of Turbulence Model Selection on the Prediction of Complex Aerodynamic Flows," AIAA Paper 79-0070, 1979.

[17] MacCormack, R. W., "An Efficient Numerical Method for Solving the Time-Dependent Compressible Navier-Stokes Equations at High Reynolds Number," *Computing in Applied Mechanics,* ASME, AMD, Vol. 18, 1976.

[18] Liou, M-S., Coakley, T. J., and Bergmann, M. Y., "Numerical Simulation of Transonic Flows in Diffusers," AIAA Paper 81-1240, 1981.

[19] Favre, A., "Equations des Gaz Turbulents Compressibles," *Journal of Fluid Mechanics,* Vol. 4, No. 3, 1965, pp. 361-390.

[20] Baldwin, G. S. and Lomax, H., "Thin-Layer Approximation and Algebraic Model for Separated Turbulent Flows," AIAA Paper 78-257, 1978.

[21] Wilcox, D. C. and Rubesin, M. W., "Progress in Turbulence Modeling for Complex Flow Fields Including Effects of Compressibility," NASA TP1517, 1980.

[22] Viegas, J. R. and Horstman, C. C., "Comparison of Multiequation Turbulence Models for Several Shock-Separated Boundary Layer Interaction Flows," AIAA Paper 78-165, 1978.